Arch. Metall. Mater. **66** (2021), 1, 249-258

DOI: 10.24425/amm.2021.134782

G. REYES-CASTELLANOS[1*], A. CRUZ-RAMÍREZ[2], E. COLIN-GARCÍA[1],
V.H. GUTIÉRREZ-PÉREZ[3]

THERMODYNAMIC ANALYSIS OF THE GRAPHITE FLAKE FORMATION OF LOW MANGANESE AND SULFUR GRAY CAST IRON

Low manganese and sulfur gray irons were produced by adding inoculant base Fe-Si with small amounts of Al and Ca in the ladle. The effect of the cast thickness, inoculant amount and shakeout time of the green sand molds were studied on the graphite flake formation by microscopically techniques. A thermodynamic analysis was carried out for the cast iron produced with the FactSage 7.2 software. Stability phase diagrams were obtained for both gray cast irons to different manganese (0.1 to 0.9 wt.%) and sulfur (0.01 to 0.12 wt.%) amounts to 1150°C. It was shown that lower amounts of manganese and sulfur allow forming the $3Al_2O_3 \cdot 2SiO_2$, Al_2O_3, and ZrO_2 solid compounds. The thermodynamic results match with those obtained by SEM-EDS. It is possible to form MnS particles in the liquid phase when the solubility product (%Mn) × (%S) equals 0.042 and 0.039 for heats A and B, respectively.

Keywords: Gray iron, inoculation, cell count, thermodynamic analysis

1. Introduction

Historically, gray cast irons were melted in cupola furnaces with high levels of sulfur but they have been replaced by a new generation of coreless induction furnaces which improved iron quality for large scale production [1]. Even with coreless induction furnaces, foundry practice can be varied so that nucleation and growth of graphite flakes occur in a pattern that enhances the desired properties. The nucleation of graphite in cast iron has been researched by many decades and, consequently, many theories regarding graphite nucleation have been proposed [2]. A high liquid iron undercooling is required to form smaller sizes micro cluster that acts as stable homogeneous nuclei for graphite particles; however, such high undercooling is very difficult to achieve in common foundry practices; therefore, the nucleation of graphite is mainly carried out by heterogeneous nucleation [3]. Inoculation is required during the liquid metal pouring of the casting in order to obtain graphite flakes. Inoculants are ferrosilicon alloys which may contain Al, Ca, Ba, Sr, Zr, Rare Earths, as well known as inoculant elements that promote and participate in the creation of micron-sized active compounds in the melt, to act as effective graphite nucleation sites [4]. So, inoculants are added to produce heterogeneous nucleation of these graphite flakes and obtain the desired distribution of them. These inoculants produce heterogeneities in the form of oxides and sulfides to enhance the nucleation of graphite on oxysulfide particles. Based on the Gibbs free energy of formation at 1723 K ($\Delta G°_{1723K}$) of oxides, silicates, nitrides, and carbides, the oxides allow more stable particles followed by the sulfides to form in commercial iron melts, than with nitrides and carbides, respectively [1]. It has been found that three groups of elements play an important role in nucleating graphite in industrial gray cast irons: a) Al and Zr, as strong deoxidizing elements promote early forming microinclusions; b) Mn and S to support MnS type sulfide formation; and c) Ca, Ba and Sr, as inoculating elements act in the first stage by forming various oxides that can subsequently nucleate sulfides and in the second stage by changing the lattice parameters of the subsequently nucleated (Mn,X)S compounds [5-7]. The amount of inoculant added are in the range from 0.05 to even 1.0 wt.% of the mass metal and depends on the carbon equivalent, sulfur levels, thin sections of casting, raw materials and the time at which the inoculant is added relative to the melting process [8,9]. The Standard ASTM A247 establishes a test method that covers the classification of graphite in cast irons in terms of type, distribution, and size by visual comparison to reference photomicrographs.

[1] DEPARTAMENTO DE INGENIERÍA EN METALURGIA Y MATERIALES. INSTITUTO POLITÉCNICO NACIONAL – ESIQIE. UPALM. CIUDAD DE MÉXICO. MÉXICO
[2] DEPARTAMENTO DE FORMACIÓN BÁSICA DISCIPLINARIA. INSTITUTO POLITÉCNICO NACIONAL – UPIIH – ESIQIE. PACHUCA, MÉXICO
[3] DEPARTAMENTO DE FORMACIÓN ESPECÍFICA. INSTITUTO POLITÉCNICO NACIONAL – UPIIZ. ZACATECAS, MÉXICO

* Corresponding author: g_reyes95@hotmail.com

There are five graphite distributions, from type-A to type-E where a type-A graphite distribution is the structure desired if mechanical properties are to be optimized [10]. Another parameter that affects graphite morphology is the solidification velocity or the cooling rate. Lacaze et al [11] determined that type-A graphite forms at low solidification velocities. As the velocity increases, a transition to type-D graphite will occur. It is now widely accepted that in S and Mn-containing lamellar graphite irons, graphite lamellar nucleates on MnS complex compounds which have low crystallographic misfit with the graphite [12]. The manganese sulfides contain additional elements such as Al (as Al_2O_3) and Mg (as MnMgS) if the melt contains small amounts of Mg [13]. It has been reported [7,14,15] that Mn and S were found as (Mn,X)S complex compounds in all micro-inclusions found in commercial irons, regardless of their position in the iron structure, iron chemistry, or iron melt treatment. The (Mn,X)S complex compounds appear at a lower Mn/S ratio and with higher compatibility for graphite nucleation, especially when one or more of these inoculating elements – Ca, Sr, Ba are present. However, Muhmond and Fredriksson [2] reported that nucleation of MnS in the melt depends on the solubility product of Mn and S and does not depend on the Mn/S ratio. In order to obtain consistent inoculation in grey irons, it is required the control factor (%Mn) × (%S) = 0.03-0.06 meets these ranges: 0.4-1.2 wt.%Mn and 0.04-0.12 wt %S, with 0.005-0.010 wt.%Al and/or Zr [1]. However, gray cast iron can be obtained for low manganese and sulfur amounts, especially for ferritic irons.

In the present work, two hypo-eutectic gray cast irons with low Mn, S and Si contents were fabricated. Casting samples of 25.4 and 12.7 mm in thickness were obtained from the heats produced in green sand molds shakeout at times of 10, 20 and 30 minutes to evaluate the microstructural features of the graphite flake formation by optical microscopy and scanning electron microscopy (SEM) with energy dispersive spectra (EDS). A thermodynamic analysis with the commercial software FactSage 7.2 was carried out to predict the compounds formation which was represented in the stability phase diagrams considering the chemical composition of the heats produced to different manganese (0.1 to 0.9 wt.%) and sulfur (0.01 to 0.12 wt.%) contents to 1150°C.

2. Experimental methods

Two hypo-eutectic gray cast irons, identified as A and B for the low and high silicon content, respectively, were produced in a 50 kg medium-frequency coreless induction furnace and cast in green sand molds. The system sand used in the study was a recycled green sand with 60 AFS GFN silica sand, 3.5% moisture and 1% sodium bentonite. The base iron was prepared with a mixture of low C and Mn steel and pig iron as the metallic charge. High purity carbon riser and FeSi (75%) were used to adjust the chemical composition of the charge. Table 1 shows the chemical composition of raw materials. The base iron was inoculated by 0.5 and 1.4 wt.% commercial foundry grade FeSi (72 wt.% Si + 1.3 wt.% Al and 1.13 wt.%Ca) for heat A and B, respectively at 1450°C. The inoculation was performed by the ladle inoculation method, where the inoculant was added to the metal stream as it flowed from the induction furnace into a pouring type shank ladle (21 cm I.D., 20 cm deep) at 1450°C.

TABLE 1

Chemical composition of the raw materials for the melts

Material	Chemical composition (wt.%)					
	C	Si	Mn	P	S	Fe
1018 Steel	0.19	0.23	0.40	0.035	0.014	Balance
Pig Iron	3.94	0.079	0.028	0.04	0.03	Balance
Graphite	99	—	—	—	0.05 max.	—
FeSi	—	75	—	—	-	Balance

The cast iron was poured at 1400°C in three green sand molds for each heat previously prepared to obtain plates of 120 × 40 mm and a thickness ranging from 25.4 to 4.23 mm by using the pattern showed in figure 1. The three sand molds were shakeout at 10, 20 and 30 minutes, respectively, after the pouring of the liquid metal into the molds for each heat. The microstructural and mechanical analysis was carried out from samples obtained from the cast plates of 25.4 and 12.7 mm in thickness (plates A and D from Fig. 1).

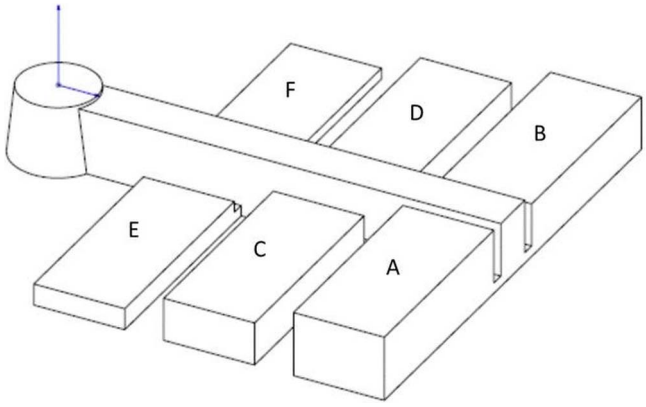

Fig. 1. Pattern design with plates of six different thickness

The nominal chemical composition in the castings was analyzed by an Oxford spark emission optic spectrograph and the reported values in Table 2 are the average of five measurements on each heat.

TABLE 2

Chemical compositions of the heats

Heat	wt. %							Mn × S	CE
	C	Si	Mn	P	S	Al	Zr		
A	3.61	1.12	0.176	0.033	0.032	0.004	0.004	0.005	3.99
B	3.34	2.11	0.159	0.044	0.042	0.017	0.010	0.006	4.06

CE = %C + 1/3%Si + 1/3%P; Balance Fe

In terms of microstructural examinations, standard metallography was employed using an optical microscope Olympus PMG-3 model according to the standard ASTM A247 to evaluate the size and distribution of the graphite flakes. High definition images of graphite flakes were taken with a scanning electron microscope (SEM) JEOL model 6701 F. Images were obtained to different magnifications with backscattering electrons of 15 kV. The micrographs were analyzed of particles located at edges and tips of the graphite flakes with the Energy Dispersive Spectra (EDS) analysis, looking for the presence of inoculant elements (Al and Ca) contained in the inoculants added and MnS particles formed.

The eutectic cell characteristics were evaluated for the samples shakeout at 30 min and the thickness of 25.4 mm with the Steads reagent (2.5 g $CuCl_2$, 10 g $MgCl_2$, 5 ml HCl, 250 ml ethanol) and the metallographic procedure reported by J. Radzikowska [16]. The samples were heat treated to 705°C for 60 min, and then quenched in water. Afterward, the samples were etched for 120 min in order to reveal clearly the eutectic cells [17] and its count was performed according to the procedure reported by Fras and López [18].

3. Thermodynamic modeling

FactSage version 7.2 [19] with the module Equilib was used to determine the concentration of the different chemical species once they reach the chemical equilibrium state. The user gives the initial amount of chemical elements, the temperature and the pressure of the system (usually 1 atm), then the program calculates the most stable species with the Gibbs free energy minimization method. In order to obtain the stability phase diagram of compounds formed, the chemical composition of each heat reported in Table 2 was considered. The computer simulation was carried out using the Liquid Fe database contained in the FTMisc Database and FToxid database. The oxygen dissolved in the liquid iron was set in 0.005% considering the estimated reported by Hughes [20] and the oxygen measurements reported by Sommerfeld [21]. The stability phase diagrams were obtained from 0.01 to 0.12% S and from 0.1 to 0.9% Mn which cover the typical amounts found in commercial gray cast irons. The stability phase diagrams were evaluated to 1150°C just before solidification. In addition, the phases formed and its quantity during solidification from 1450 to 1050°C were determined for the chemical composition of heats A and B. The thermodynamic properties of the pure oxides, silicate, and sulfides compounds considered in the thermodynamic simulation are given in Table 3.

4. Results and discussion

4.1. Chemical composition

The nominal chemical composition analyzed in the castings (Table 2) was determined with an Oxford spark emission optic equipment. The carbon equivalent (CE) values show that the cast irons obtained correspond to hypo-eutectic gray cast irons. The manganese and sulfur contents were kept low for both heats. The silicon content was kept low for heat A and an optimum value for heat B in order to enhance the amount of inoculant added to the melt.

4.2. Optical Microscopy

The metallurgical microstructures of the gray cast iron samples produced by adding 0.5 and 1.4 wt.% of the commercial inoculant FeSi (72 wt.% Si + 1.13 wt.%Ca and 1.3 wt.% Al) are shown in Fig. 2 and Fig. 3 for the three shakeout times and two thickness considered.

Fig. 2 shows the microstructures of heat A produced adding 0.5 wt.% of the commercial inoculant. It can be seen that heat A mainly contents type-E graphite in all the cases evaluated. It is also evident that the samples of 25.4 mm in thickness show

TABLE 3

Thermodynamic Properties Relative to Elements and Compounds at 298.15 K

$$H(\mathrm{J\,mol^{-1}}) = A + \int_{298.15}^{T} C_p dT \; ; \; S(\mathrm{J\,mol^{-1}\,K^{-1}}) = B + \int_{298.15}^{T} \left(\frac{C_p}{T}\right) dT$$

$$Cp(\mathrm{J\,mol^{-1}\,K^{-1}}) = a + b(10^{-3})T + c(10^{5})T^{-2} + dT^{-1/2} + e(10^{8})T^{-3}$$

	A	***B***	***a***	***b***	***c***	***d***	***e***
Al_2O_3 (l)	–1596,353.1	43.5690	179.3655	—	–9.192E–8	975,340.9	–828.3E–8
Al_2O_3 (α)	–1675,700.0	50.81998	155.0188	—	–38.6136	–828.386	4.090836
MnS (l)	–188,715.7	92.32288	47.6976	—	7.5312E–8	66.944	—
MnS (a)	–214,200.0	78.1990	47.6976	—	7.5312E–8	—	—
Fe (l)	21,189.62	43.4219	23.51430	—	8.795E–8	–154,717	3.535E–15
Fe (fcc)	7,973.03	35.90209	24.66430	—	7.515E–8	–154,717	3.535E–15
ZrO_2 (l)	–1031,019.0	50.6701	87.8640	—	—	—	—
ZrO_2 (m)	–1097,462.9	50.3590	94.6211	—	–5.844E–3	–1.204E8	—
Zr_2S_3 (s)	–1019,222.4	125.5200	121.3360	—	—	—	—
$3Al_2O_3{\cdot}2SiO_2$ (m)	–6819,209.9	274.9001	634.8099	—	–172.0990	–3373.500	21.22740

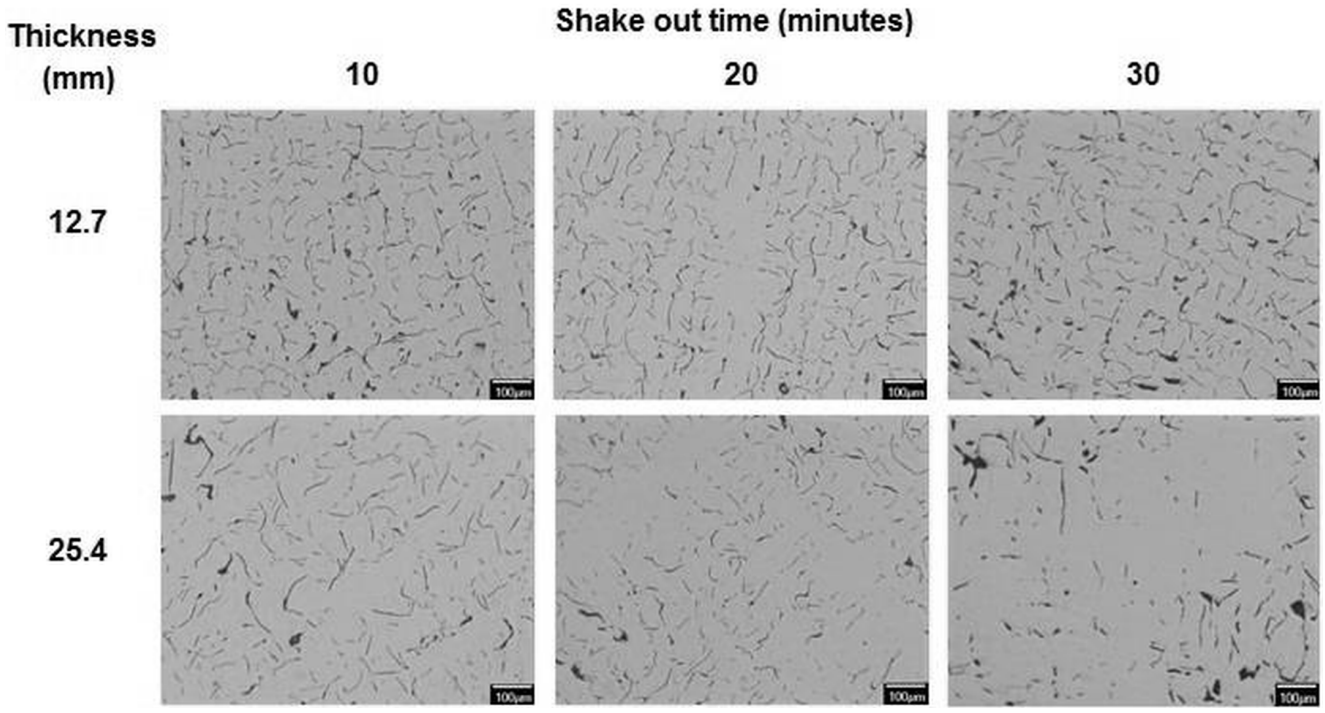

Fig. 2. Unetched microstructure for the 12.7 mm and 25.4 thickness plates after the shakeout time of 10 min., 20 min., and 30 min. of heat A

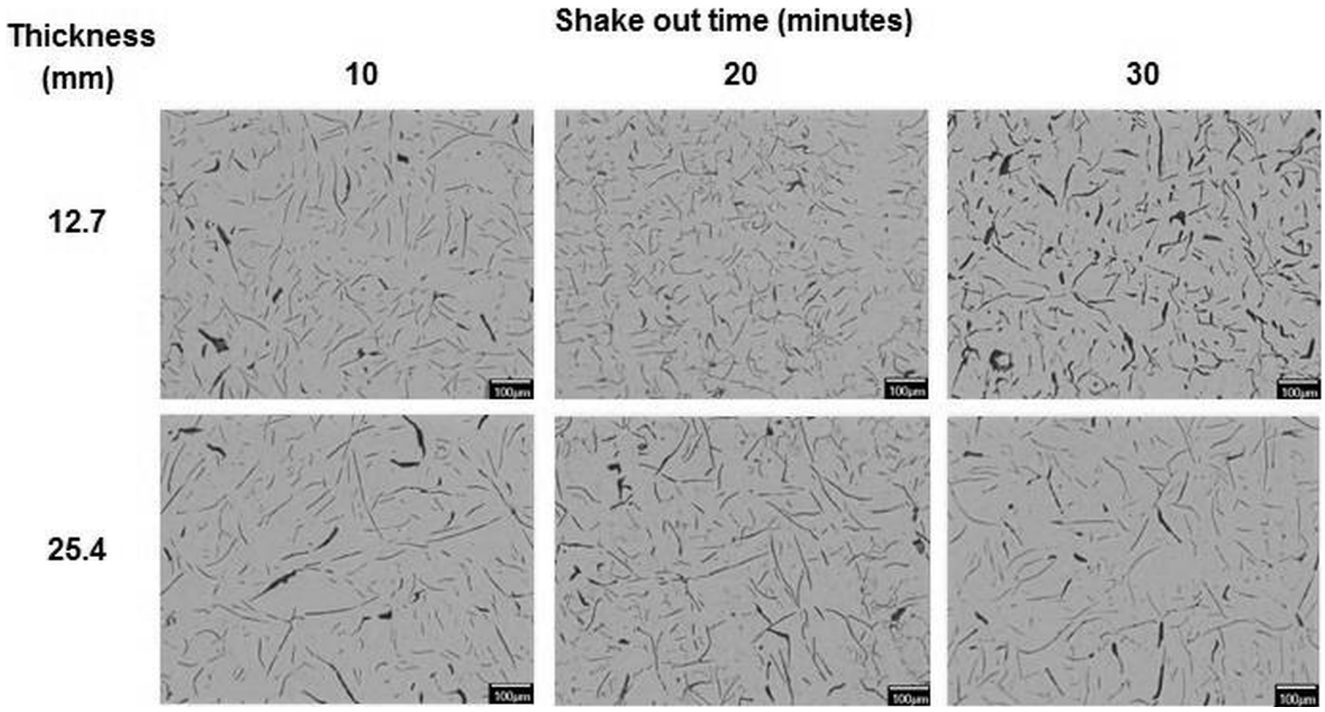

Fig. 3. Unetched microstructure for the 12.7 mm and 25.4 thickness plates after the shakeout time of 10 min., 20 min., and 30 min. of heat B

wide zones without the presence of graphite flakes. For heat A, the low silicon content in the base metal and the low amount of the commercial inoculant added, provided a poor distribution of the inoculating elements contained in the commercial inoculant to create nucleation sites for the graphite flakes, therefore, regions without graphite flakes are evident.

Fig. 3 shows microstructures of heat B produced adding 1.4 wt.% of the commercial inoculant. Heat B shows mainly types A + E and A graphite distributions for the samples of 12.7 mm and 25.4 mm in thickness, respectively. Type-A graphite distribution is desired in most of the cast iron applications. The samples of 25.4 mm in thickness for heat B show type-A graphite randomly distributed with longer graphite flakes than those obtained in heat A due to the higher silicon content in heat B.

Table 4 summarizes the graphite flake features according to the standard ASTM A247. It is observed for both heats that

TABLE 4

Average structure characteristics of gray cast irons produced

Cast	Shake out time (minutes)	Thickness (mm)	Graphite distribution	Average graphite size (μm)	Graphite size class
A	10	12.7	E	55.7	4 (30%), 5 (30%), 6 (30%), 7 (10%)
		25.4	E	63.9	4 (24%), 5 (52%), 6 (20%), 7 (4%)
	20	12.7	E	59.9	4 (30%), 5 (40%), 6 (30%)
		25.4	E	66.9	4 (16%), 5 (76%), 6 (8%)
	30	12.7	E	69.4	4 (30%), 5 (65%), 6 (5%)
		25.4	E	74.7	3 (5%), 4 (30%), 5 (55%), 6 (10%)
B	10	12.7	E	67.2	4 (35%), 5 (55%), 6 (10%)
		25.4	A	82.0	3 (5%), 4 (35%), 5 (50%), 6 (10%)
	20	12.7	A + E	66.6	4 (30%), 5 (50%), 6 (20%)
		25.4	A	82.9	3 (8%), 4 (24%), 5 (68%)
	30	12.7	A + E	68.6	4 (35%), 5 (60%), 6 (5%)
		25.4	A	100.5	3 (10%), 4 (62.5%), 5 (22.5%), 6 (5%)

the average graphite size is increased when the shakeout time is increased and this behavior is more remarkable for the thickness of 25.4 mm. For the same cooling conditions, it is also observed that higher silicon contents in heat B allow to obtain a type-A graphite distribution with longer graphite flakes reaching an average length of 100.5 μm instead of 74.7 μm and a type-E graphite distribution for heat A, corresponding to the thickness of 25.4 mm and a shakeout time of 30 minutes.

It is observed that the samples of 25.4 mm in thickness show a type-A graphite while the samples of 12.7 mm show a transition from type-A to type-E graphite distribution for heat B. The differences in the graphite morphology are attributed to the different cooling rate of the samples, there is a lower solidification rate for the samples of 25.4 mm than the samples of 12.7 mm in thickness. The center of the plates of 25.4 mm remains hotter than the ones of 12.7 mm or the external surface, therefore, a major graphite formation is induced for the thicker sample [22], the super-cooling degree of the molten iron was small and graphite had excellent nucleation ability to form type-A graphite. Lacaze et al [11] reported that a type-A graphite distribution forms at low solidification rates and as the rate increases, a transition of type-D graphite distribution will occur.

Fig. 4 shows the eutectic cell features for the samples shakeout at 30 min and the thickness of 25.4 mm for both heats. It is observed that eutectic cell count is influenced by the effects of inoculation on the solidification pattern. It is shown that, the heat A (Fig. 4a) produced with the lowest amount of inoculant contain a eutectic cell count of 7.75 cells/mm^2, while heat B (Fig. 4b) shows an increase in the eutectic cell count of 10.25 cells/mm^2, due to the higher amount of inoculant added.

4.3. Scanning Electron Microscopy

Edges and tips of the graphite flakes of the two castings produced were analyzed with the SEM-EDS technique. Fig. 5 shows a microanalysis pattern spectrum taken from a graphite flake edge of a heat B sample. The region analyzed shows mainly the presence of aluminum and calcium as the inoculant elements contained in the commercial inoculant.

Fig. 6 shows the qualitative chemical composition of the matrix and a graphite flake tip of heat A. The micrographs were taken with the backscattered electron signal, which provides direct information on compositional heterogeneity through the mechanism of atomic number contrast [23].

The EDS analysis shows that the matrix mainly contains iron, manganese, and sulfur with small quantities of calcium. In

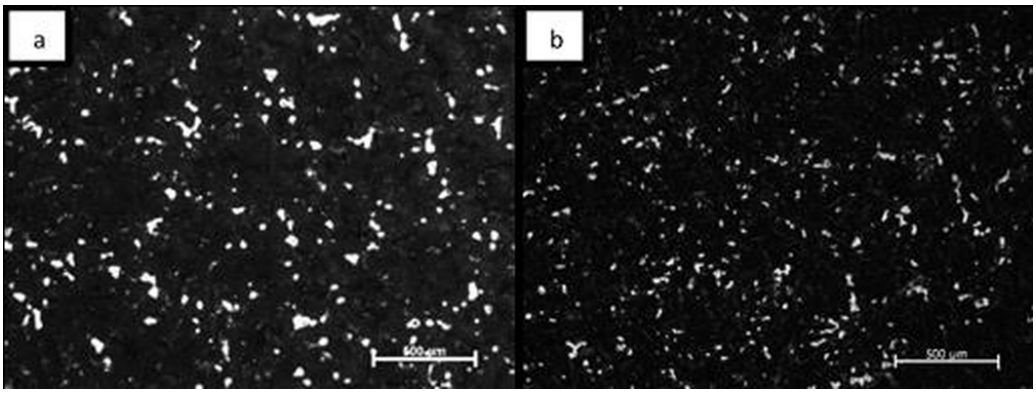

Fig. 4. Eutectic cell features for the samples of 25.4 mm in thickness shakeout at 30 min for a) Heat A and b) Heat B

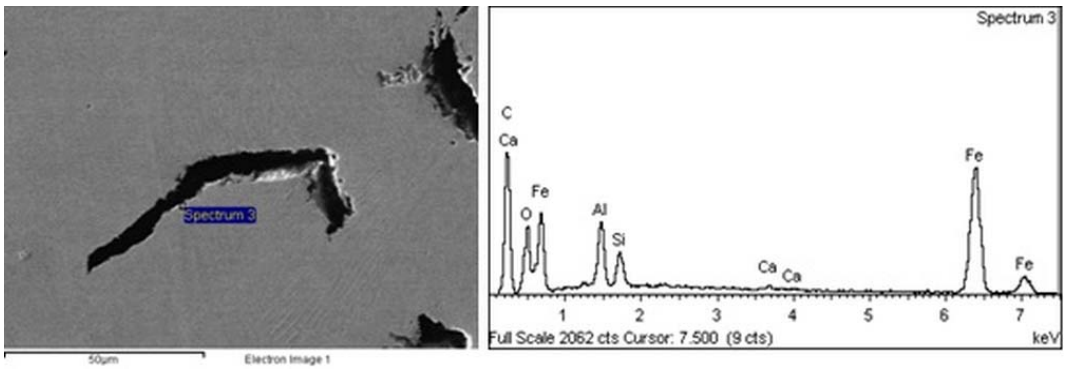

Fig. 5. SEM analysis of a graphite flake edge for heat B

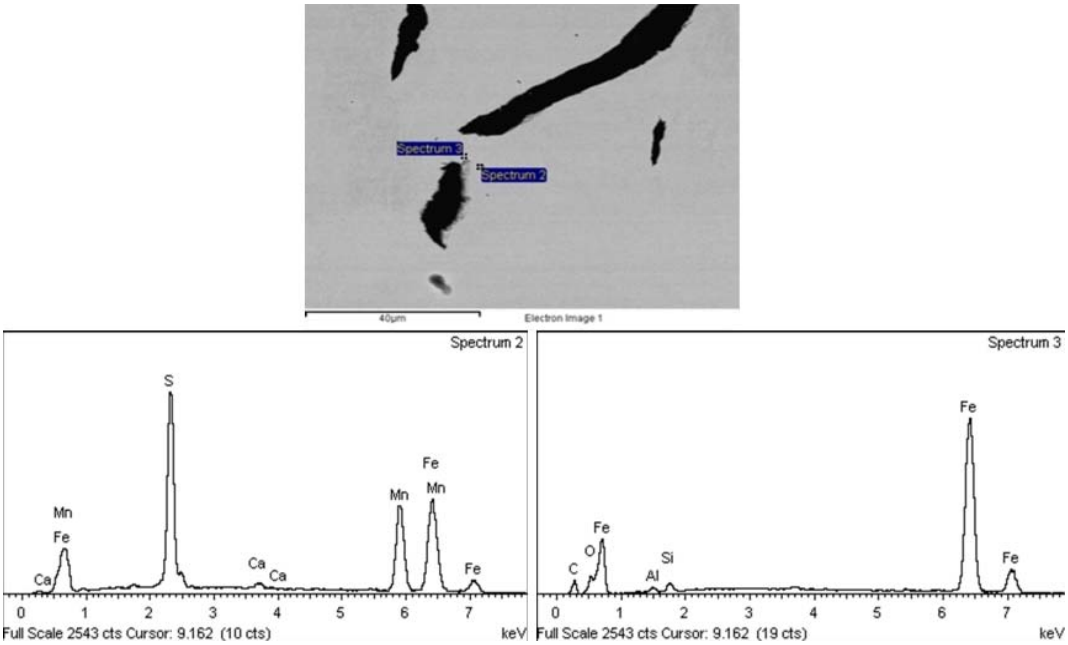

Fig. 6. SEM analysis of a graphite flake particle and tip and matrix for heat A

spite of the high concentration of manganese and sulfur at this region, a graphite flake was not formed. The particle analyzed in the tip of the graphite flake shows the presence of aluminum and oxygen which may form an alumina particle.

Fig. 7 shows a microanalysis pattern taken from a graphite flake edge of heat B. This region shows a high amount of silicon followed by the inoculant elements aluminum and calcium.

Fig. 8 shows the elemental mapping of the elements of the SEM image of Fig. 7. This technique allows us to appreciate the relative spatial relationship between the elemental constituents in a microstructure from the same area [23]. Matrix elements (C, Si, O, Fe, S, and Mn) and the inoculant elements (Al and Ca) were identified. The elemental mapping results show that the sulfur and manganese are distributed in the matrix.

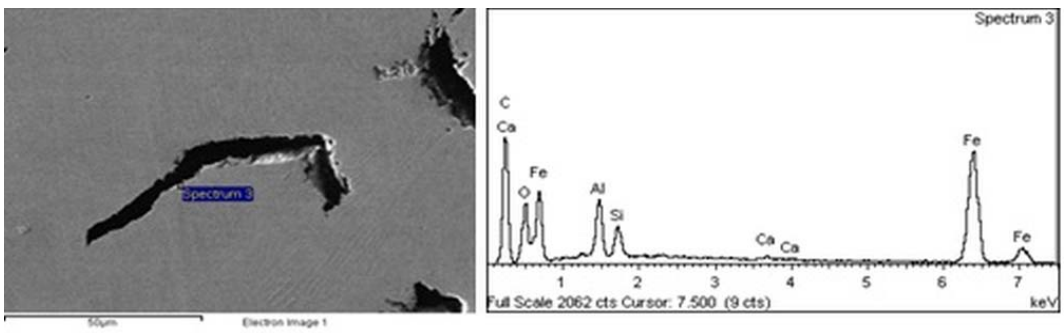

Fig. 7. SEM analysis of a graphite flake edge for heat B

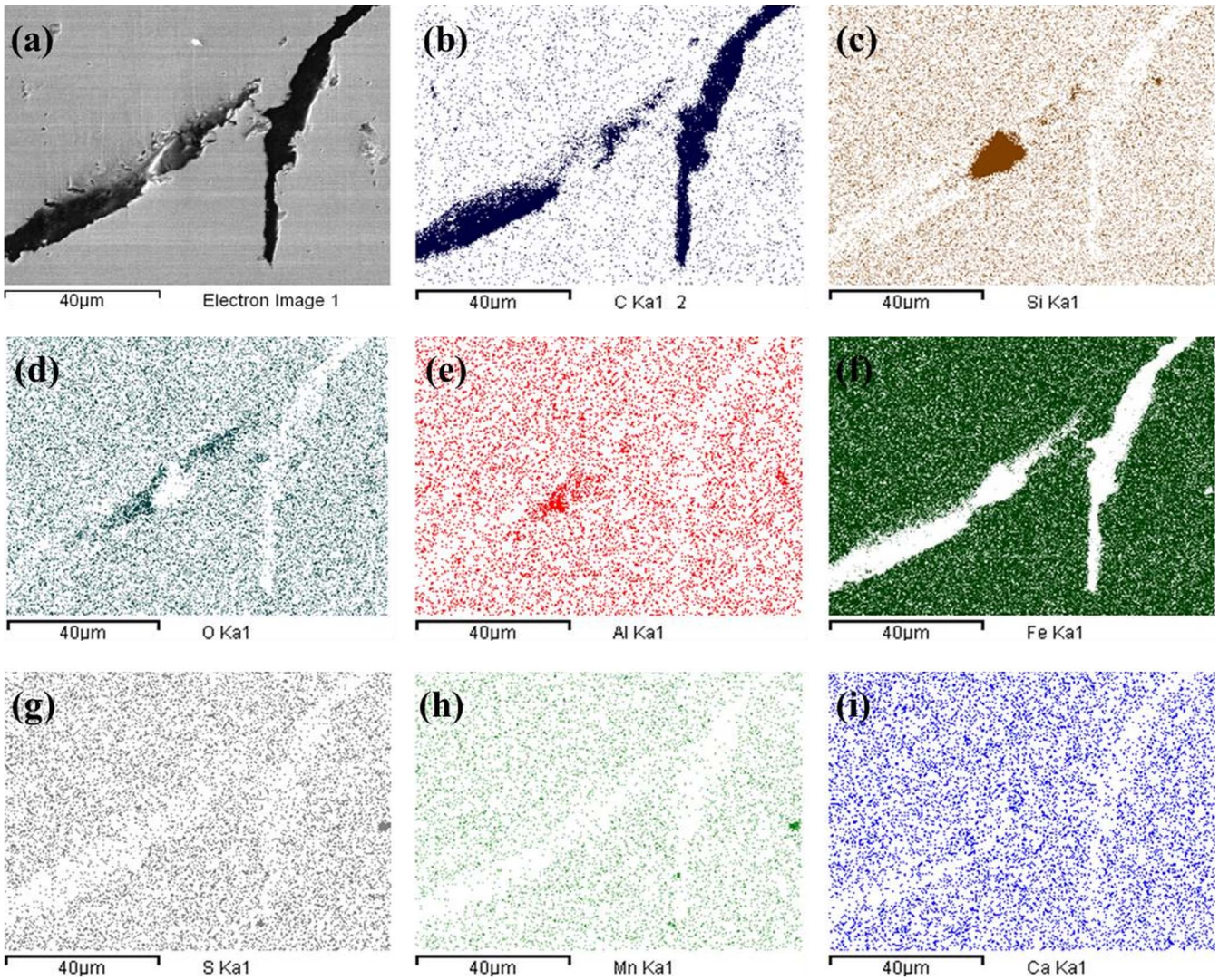

Fig. 8. SEM image (a) and SEM microanalysis. Carbon (b), Silicon (c), Oxygen (d), Aluminum (e), Iron (f), Sulfur (g), Manganese (h) and Calcium (i) were detected for heat B

4.4. Stability phase diagrams

The calculated phases obtained by FactSage 7.2 [19] with the module Equilib considering the chemical composition of the heats A and B to different manganese and sulfur contents are represented in the stability phase diagrams of Fig. 9 and Fig. 10, respectively to 1150°C. Fig. 9 and Fig. 10 also show the values of %Mn × %S across the borderline of the two main phase regions and the %Mn × %S average value of each heat. The phases identified with the thermodynamic prediction for the chemical composition of heat A to different contents of sulfur and manganese to 1150°C (Fig. 9) show a variety of phases which are: corundum (Al_2O_3), zircon oxide monoclinic (ZrO_2), mullite ($3Al_2O_3 \cdot 2SiO_2$), alabandite (MnS) and a liquid phase.

Fig. 10 shows the thermodynamic prediction for the chemical composition of heat B to different contents of sulfur and manganese to 1150°C. It is observed from Fig. 10, the formation of corundum (Al_2O_3) to lower amounts of manganese and sulfur and the formation of corundum (Al_2O_3) and alabandite (MnS)

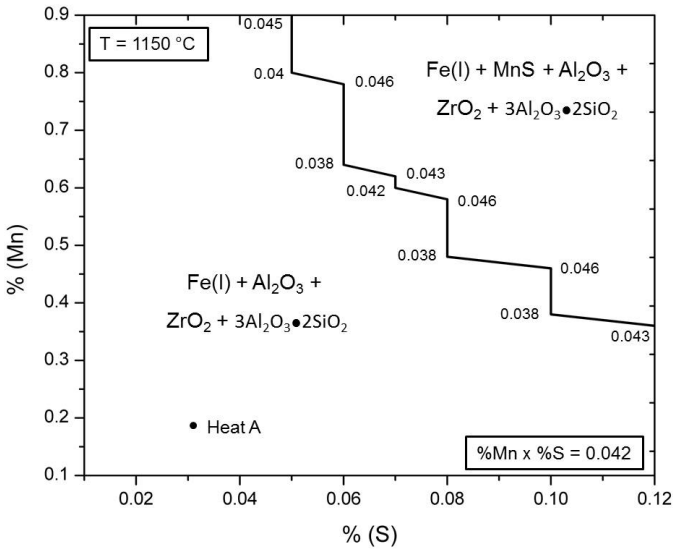

Fig. 9. Stability phase diagram of heat A to different Mn and S contents at 1150°C. Values represent the factor %Mn × %S to different Mn and S contents and it shows the %Mn × %S average value. The solid circle represents the chemical composition of Heat A

when the contents of manganese and sulfur are increased. Both regions in the stability phase diagram contain a liquid phase. According to the chemical composition in heat B, the zircon oxide monoclinic (ZrO_2) and mullite ($3Al_2O_3 \cdot 2SiO_2$) phases were not formed in spite of the higher amounts of silicon and zircon in the chemical composition of heat B (Table 2). This behavior is attributed to the higher aluminum content in heat B than in heat A, aluminum as a stronger deoxidizer reacts with the oxygen in the bath to form stable particles of alumina.

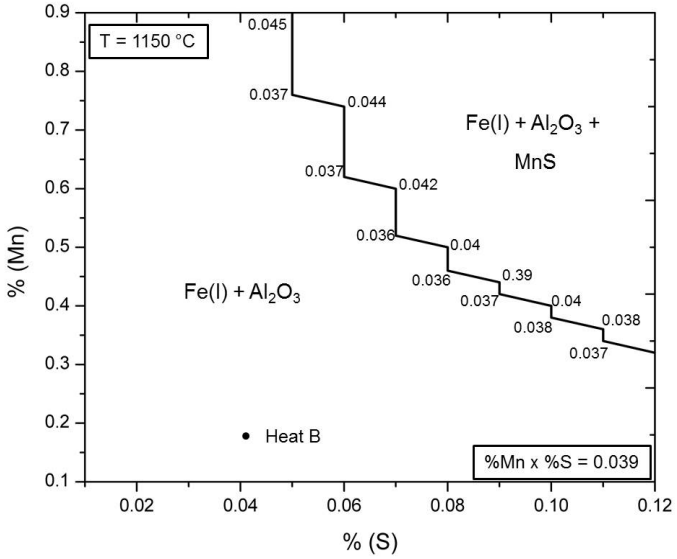

Fig. 10. Stability phase diagram of heat B to different Mn and S contents at 1150°C. Values represent the factor %Mn × %S to different Mn and S contents and it shows the %Mn × %S average value. The solid circle represents the chemical composition of Heat B

The stability phase diagrams of Fig. 9 and Fig. 10 show the fixed chemical composition of heat A and B, respectively (represented by a solid circle in Fig. 9 and Fig. 10). It is evident that these chemical compositions allow obtaining oxides (Al_2O_3, ZrO_2) and silicates ($3Al_2O_3 \cdot 2SiO_2$) instead of sulfides like the alabandite (MnS). In general, it is observed from both stability phased diagrams that higher manganese and sulfur contents are required to form the alabandite MnS phase. It was determined from both stability phase diagrams that the borderline between the main two-phase regions requires a minimum value of %Mn × %S = 0.0422 and 0.039 in average for heat A and B, respectively to form the MnS phase.

Fig. 11 and Fig. 12 show the phases formed and its quantity during solidification from 1450 to 1050°C for the chemical composition of heat A and B, respectively. Fig. 11 shows at high temperature (1450°C) the formation of $3Al_2O_3 \cdot 2SiO_2$ followed by ZrO_2 and Al_2O_3, these solids phases represent only 0.01% with 99.99% of liquid phase, when the temperature decrease to 1050°C, the amount of solid phase is increased, the $3Al_2O_3 \cdot 2SiO_2$ phase is consumed with the increase of the ZrO_2 and Al_2O_3 phases. In addition, to 1050°C, the MnS phase is formed which means that oxides and silicates are mainly formed just before solidification and then, the MnS is formed after the eutectic reaction occurs. The software predicts the formation Fe (fcc) and considers that the carbon in excess forms Fe_3C to 1050°C, however, most of the carbon must form the graphite precipitates in gray iron. Heat B (Fig. 12) shows that the main solid phase formed from 1450 to 1050°C is Al_2O_3 and when solidification occurs, the Zr_2S_3 and Fe_3C phases are formed to 1050°C. Heat A shows a higher amount of solid compounds at 1050°C than Heat B, this behavior is attributed to the difference of the silicon content in both heats, as the silicon content in the Fe-C-Si ternary system increases, the eutectic and eutectoid temperatures increase [24], therefore, the solid phases formed decreased, as can be observed in Fig. 11 and Fig. 12.

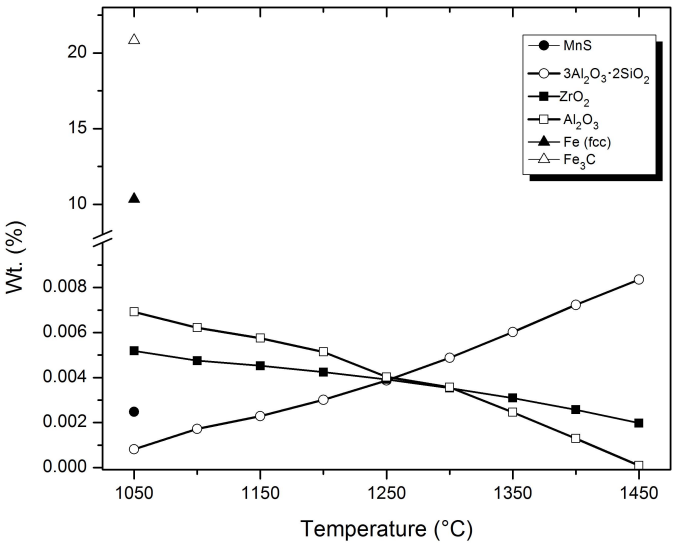

Fig. 11. Phases formed during the solidification of Heat A. Lines represent the weight % of each solid phase formed. The balance corresponds % liquid in the system at each temperature

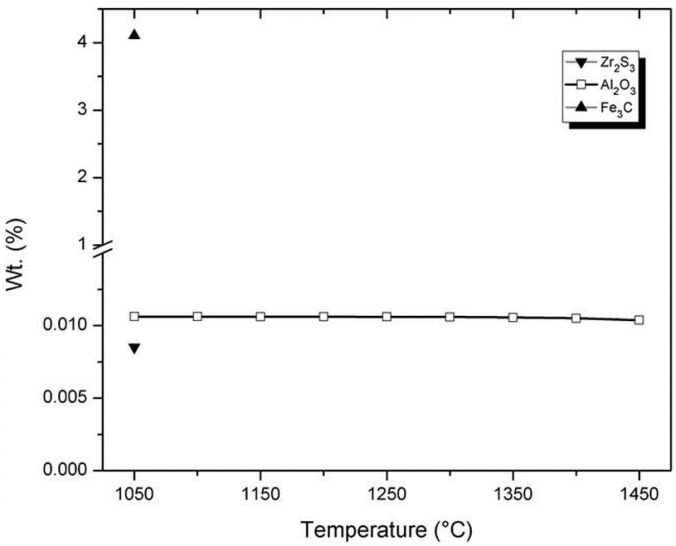

Fig. 12. Phases formed during the solidification of Heat B. Lines represent the weight % of each solid phase formed. The balance corresponds % liquid in the system at each temperature

It is observed that the Al_2O_3 formed in heat B is higher than in heat A, according to the Gibbs free energy, oxides show lower values than sulfides allowing that the oxygen in the melt reacts with stronger deoxidizers like Al and Zr to form Al_2O_3, ZrO_2 and $3Al_2O_3 \cdot 2SiO_2$ phases in the liquid phase, then as solidification proceeds, these oxides will provide nucleation sites for the MnS and Zr_2S_3 formation.

The SEM examinations in both heats showed the identification of aluminum and calcium as the inoculant elements which may form oxides that act as graphite nuclei and could not identify any MnS particle to act as graphite nuclei. As can be observed from Fig. 9 and Fig. 10, the low manganese and sulfur cast irons contained in heat A and B are located in the region where MnS particles are not formed. These results are in agreement with the results reported by Alonso et al [25] where there was no evidence on the MnS formation on early solidification samples of quenched irons with low sulfur (0.01%S) contents, giving a (%Mn) × (%S) value of 0.005 in average. For foundry application, it is recommended [15,26] to ensure the (Mn,X)S compound formation, a control factor (%Mn) × (%S) equals 0.03-0.06 and 0.005-0.01 %Al and/or Zr residual contents in inoculated gray irons. The stability phase diagrams show that the (%Mn) × (%S) values for heat A and B are 0.042 and 0.039, respectively which match with the values recommended to obtain sulfide compounds.

The inoculants added to the low manganese and sulfur cast irons produced oxides in the melt. Heat B obtained the highest eutectic cell count due to the higher amount on inoculant added, the oxides formed provides nucleation sites for MnS and Zr_2S_3 particles that are formed after the eutectic reaction occurs, the predicted results reported in Fig. 11 and Fig. 12 shows that this behavior occurs at 1050°C.

5. Conclusions

A thermodynamic analysis was carried out in the production of low manganese and sulfur hypo-eutectic gray cast irons. The stability phase diagrams obtained show that the predicted phases formed Al_2O_3, ZrO_2 and $3Al_2O_3 \cdot 2SiO_2$ provide nucleation sites in the liquid phase and as solidification proceeds, the MnS and Zr_2S_3 phases are formed. Nucleation of the MnS in the liquid phase depends that the solubility product (%Mn) × (%S) equals 0.042 and 0.039 for heats A and B, respectively. The thermodynamic prediction match with the SEM-EDS results where Al and Ca particles were mainly detected attached to the graphite flake formation, these particles may form alumina that acted as graphite nuclei. The eutectic cell count is strongly influenced by the effects of inoculation on the solidification pattern. The heat A produced with the lowest amount of inoculant shows a low eutectic cell count while heat B shows a strong increase in the eutectic cell count due to the higher amount of inoculant added. Heat B shows mainly types A + E and A graphite distribution for the samples of 12.7 mm and 25.4 mm in thickness, respectively; while the casting produced with the lowest amount of inoculant showed a type E graphite distribution for all the samples evaluated. The average graphite size was increased when the shakeout time was increased and mainly when the thickness plate was increased.

Acknowledgments

The authors wish to thank the Institutions CONACyT, SNI and SIP-Instituto Politécnico Nacional for their permanent assistance to the Process Metallurgy Group at ESIQIE-Metallurgy and Materials Department.

REFERENCES

[1] I. Riposan, M. Chisamera, S. Stan, ISIJ Int. **53**, 10, 1683-1695 (2013), DOI: 10.2355/isijinternational.53.1683.

[2] H.M. Muhmond, H. Fredriksson, Metall. and Mater. Transactions B **44B**, 283-298 (2013), DOI: 10.1007/s11663-012-9768-6.

[3] I. Minkoff. The Physical Metallurgy of Cast Iron. Norwich, England, John Wiley and Sons Ltd (1983).

[4] I. Riposan, M. Chisamera, S. Stan, J. of Therm. Analysis and Calorim. **132**, 1017-1028 (2018), DOI: 10.1007/s10973-018-7023-3.

[5] I. Riposan, M. Chisamera, S. Stan, T. Skaland, M. Onsoien, Analyses of Possible Nucleation Sites in Ca/Sr Over-inoculated Gray Irons. AFS (2001).

[6] I. Riposan, M. Chisamera, S. Stan, T. Skaland, Int. J. Cast Met. Res. **16**, 105-111 (2003), DOI: 10.1080/13640461.2003.11819567.

[7] I. Riposan, M. Chisamera, S. Stan, T. Skaland, A new Approach to Graphite Nucleation Mechanism in Gray Irons. Proc. AFS Cast Iron Inoculation Conference, Schaumburg, IL, AFS (2005).

[8] I. Riposan, S. Stan, V. Uta, I. Stefan, J. of Mater. Eng. and Perform. **26**, 4217-4226 (2017), DOI: 10.1007/s11665-017-2869-2.

[9] J.R. Brown, Ferrous Foundryman's Handbook. Woburn, MA, Foseco International Ltd (2000).

[10] C.V. White, Gray Iron. ASM Handbook. Volume 1. USA, ASM International (1993).

[11] J. Lacaze, M. Aberg, J. Sertucha, Review of microstructural features of chunky graphite in ductile cast irons. Keith Millis Symposium on Ductile Iron Nashville TN, AFS (2013).

[12] L.R. De, Y.J. Xiang, Heterogeneous nuclei in flake graphite. Trans. AFS (1991).

[13] A. Sommerfeld, B. Tonn, Int. J. of Metalcasting **3** (4), 39-47 (2009), DOI: 10.1007/BF03355457.

[14] I. Riposan, M. Chisamera, S. Stan, C. Hartung, D. White, Mater. Sci. and Technol. **26**, 1439-1447 (2010), DOI: 10.1179/026708309X12495548508626.

[15] M. Chisamera, I. Riposan, S. Stan, D. White, G. Grasmo, Int. J. Cast Met. Res. **21**, 1-4 (2008). DOI: 10.1179/136404608X361639.

[16] J.M. Radzikowska, Mater. Characterization **54**, 287-304 (2005), DOI:10.1016/j.matchar.2004.08.019.

[17] G.F. Vander Vort, Metallography Principles and Practice. 4th printing. Materials Park, OH, ASM International (2007).

[18] E. Fras, H. López, Int. J. of Metalcasting **4**, 35-61 (2010), DOI: 10.1007/BF03355497.

[19] C.W. Bale, A.D. Pelton, W.T. Thompson, Facility for the Analysis of Chemical Thermodynamics (FactSage, v. 7.2), User's Manual; 2018.

[20] I.C. Hughes, Trans. AFS **77**, 121(1969).

[21] A. Sommerfeld, B. Tonn, Int. J. of Cast Metals Res. **21**, 23-6 (2008). DOI: 10.1179/136404608X361602.

[22] I. Zalakain, C. Berlanga, L. Alvarez, L. Asa, P. Labé, P. Rivero, J. valencia, R. Rodríguez, J. Min. Metall. Sect. B-Metall. **54**, 91-9 (2018). DOI: 10.2298/JMMB160718012Z

[23] J. Goldstein, D. Newbury, D. Joy, C. Lyman, P. Echlin, E. Lifshin et al., Scanning Electron Microscopy and X-Ray Microanalysis. 3rd ed. New York, Springer Science+Business Media, LLC (2003).

[24] E. Piwowarsky, Hochwertiges Gusseisen. 2nd ed. New York, Springer-Verlag (1958).

[25] G. Alonso, D.M. Stefanescu, P. Larrañagara, E. de la Fuente, E. Aguado, R. Suárez, Int. J. of Cast Metals Res. **1-8** (2016), DOI: 10.1080/13640461.2016.1165459.

[26] M. Chisamera, S. Stan, I. Riposan, G. Grasmo, C. Hartung, Int. J. of Cast Metals Res. **24**, 363-9 (2011), DOI: 10.1179/1743133611Y.0000000011.